Applied Catalysis B: Environmental 336 (2023) 122923

Contents lists available at ScienceDirect

Applied Catalysis B: Environmental

journal homepage: www.elsevier.com/locate/apcatb

# Oxygen vacancy engineered molecular imprinted $TiO_2$ for preferential florfenicol remediation by electro-reductive approach: Enhanced dehalogenation performance and elimination of antibiotic resistance genes

Zimo Lou [a,b,c], Xiaofei Wen [b], Ludi Song [a,b], Chen Yan [b], Hongxu Chen [b], Tao Lu [b], Jianming Yu [a,b,*], Xinhua Xu [d,**], Jiansheng Li [c,**]

[a] Collaborative Innovation Center of Yangtze River Delta Region Green Pharmaceuticals, Zhejiang University of Technology, Hangzhou 310014, China
[b] College of Environment, Zhejiang University of Technology, Hangzhou 310014, China
[c] Key Laboratory of Jiangsu Province for Chemical Pollution Control and Resources Reuse, School of Environment and Biological Engineering, Nanjing University of Science and Technology, Nanjing 210094, China
[d] Department of Environmental Engineering, Zhejiang University, Hangzhou 310058, China

ARTICLE INFO

*Keywords:*
Molecular imprinting
Electrolysis
Halogenated antibiotics
Dehalogenation
Antibiotic resistance genes

ABSTRACT

To achieve the precision removal of trace florfenicol (FLO) with presence of various high-concentration interferents in water matrices, an oxygen vacancy engineered molecular imprinted $TiO_2$ (MI-$TiO_{2-x}$) cathode material was customized rationally. Benefiting from the increased recognition and the accelerated interfacial charge transfer contributed by molecular imprinted sites and oxygen vacancy, respectively, MI-$TiO_{2-x}$ deeply dehalogenates 10 mg $L^{-1}$ FLO via direct electron transfer with the degradation rate constant of 0.021 $min^{-1}$. Such electrode material outperforms most of the recent electrocatalysts, and show resistance to co-existing interferents (e.g. reduced sulfur species). In an electro-reductive and biological coupling system, MI-$TiO_{2-x}$ removes the antibacterial activity of 2 mg $L^{-1}$ FLO in swine wastewater and thus eliminates the abundance of FLO resistance genes. This study provides insights into not only rational design of the noble-metal-free electrocatalyst for preferential remediation of low-concentration organic halides, but also the significance of mitigating ecological risk by dehalogenation treatment.

## 1. Introduction

The globally increasing consumption of antibiotics for prevention and treatment of infectious disease has led to the growing input of antibiotics into water matrices, through their manufacturing waste streams or via excretions (urine and faces) from humans and domestic animals [1–3]. As a result, the presence of antibiotics in water poses potential risks to human health by producing antibiotic resistance genes (ARGs) and antibiotic-resistant pathogens [4,5]. Florfenicol (FLO) is a typical wide-spectrum antibiotic agent, which shows high tolerance to conventional water treatment technologies (especially biological treatment) [6]. Due to its antibacterial property and poor biodegradability, FLO can finally reach and persist in natural aquatic environment through municipal wastewater treatment plant effluents and surface runoffs [7].

Since the biological toxicity of halogenated organics primarily relies on the halogen substitutes in their molecular structure [8], dehalogenation of FLO can efficiently eliminate its antibacterial activity and thus prevent ARGs from spreading. Electro-reductive approach serves as an ideal option for dehalogenation of typical antibiotics, benefiting from its environmental friendliness, mild reaction condition and low maintenance requirements [9]. To boost the application of such technology, recent studies have developed transition metal-based cathode materials involving oxides [10], phosphides [11], sulfides [12], and enzyme-like catalysts with metal centers [13]. Although these cathode materials show high dehalogenation activity (even better than Pd), most of the studies were conducted with tens of mg $L^{-1}$ of antibiotics, which may be relevant to the concentrated waste stream with a preconcentration step (e.g. adsorption, ion exchange resins, membrane filtration). However,

* Corresponding author at:Collaborative Innovation Center of Yangtze River Delta Region Green Pharmaceuticals, Zhejiang University of Technology, Hangzhou 310014, China.
** Corresponding authors.
*E-mail addresses:* yjm@zjut.edu.cn (J. Yu), xuxinhua@zju.edu.cn (X. Xu), lijsh@njust.edu.cn (J. Li).

https://doi.org/10.1016/j.apcatb.2023.122923
Received 11 December 2022; Received in revised form 1 March 2023; Accepted 26 May 2023
Available online 27 May 2023

under most circumstances, antibiotics tends to exist at μg $L^{-1}$ level with ppm-level coexisting components [14,15]. Therefore, how to develop electrode materials targeting increased selectivity toward low-concentration antibiotics becomes an emerging topic.

Molecular imprinting (MI), as a versatile technique, enables the selective recognition of certain molecules for applications involving immunoassay, membranes and sensors, catalysis, and etc [16–18]. Based on a MI design principle, catalytic materials can accurately remove low-content pollutants in the presence of high-concentration interferents, as well as their chronic environmental risks [19]. One original method to introduce MI sites is to modify the surface of traditional catalytic materials with a coating layer of molecular imprinted polymers (MIPs) [20]. However, for electrocatalysts, the poor electrical conductivity of MIPs may increase the resistivity of electrode materials and slow down the electrode/solution interfacial charge-transfer dynamics. With these concerns, directly imprinting the targeted templates on the surface of catalytic materials is expected to be a more advanced strategy, since the modification of MIPs layer is avoided [21,22]. Interestingly, to the best of our knowledge, the report on bridging inorganic imprinting technology with electro-reductive dehalogenation is still lacking.

Titanium oxide ($TiO_2$) is by far the most widely employed semiconducting material in (photo-) electrochemical applications like sensors, ion batteries, water splitting and etc [23,24]. Nonetheless, pristine $TiO_2$ suffers from intrinsic poor conductivity and rare active sites, thus substantially restricting its catalytic performance without UV irradiation [25]. To overcome the wide band gap of pristine $TiO_2$ ($E_g = 3.0$ eV), it is engineered with surface defects like oxygen vacancies and $Ti^{3+}$, or exposed with tailored facets (e.g. high-energy {001} facets) [26,27]. Note that the creation of inorganic molecular imprinting (MI) sites on the surface of $TiO_2$ has also been achieved [28], it is reasonable to propose a novel $TiO_2$-based cathode material with co-existence of surface defects and MI sites.

In the present study, we proposed an oxygen vacancy engineered molecular imprinted $TiO_2$ (MI-$TiO_{2-x}$) for electro-reductive dehalogenation of low-concentration FLO from both simulated and real water systems. This study aims at answering: 1) how effective MI-$TiO_{2-x}$ is to dehalogenate FLO where high concentration of interferents coexist; 2) how does MI-$TiO_{2-x}$ work during the dehalogenation of FLO; 3) whether electro-reductive dehalogenation contributes to ARGs elimination. This work offers a reliable approach for advanced treatment of halogenated antibiotics in aquatic environment.

## 2. Experimental section

### 2.1. Chemicals and materials

Details of the used chemicals and materials are provided in Text S1.

### 2.2. Synthesis of electrode materials

The fabrication procedure of oxygen vacancy engineered molecular imprinted $TiO_2$ (MI-$TiO_{2-x}$) is shown in Scheme 1, derived from the traditional synthesis of $TiO_2${001} nanosheets using HF as a capping agent [29]. Firstly, molecular imprinted $TiO_2$ (MI-$TiO_2$) was prepared by hydrothermal method, followed by template removal via calcination. Briefly, 25 mL tetrabutyl titanate (TBOT) was mixed with 25 mg florfenicol (FLO) template molecules and 0.4 mL deionized (DI) water, and magnetically stirred for 30 min in a 50 mL Teflon-lined autoclave. The mixture was sonicated for another 10 min to ensure the dissolution of FLO. Then 3 mL hydrofluoric acid (HF) was added dropwise with vigorous stirring for 2 h, and the autoclave was kept at 180 ℃ for 24 h. After cooling to ambient temperature, the white gel powders were washed and centrifuged by DI water and ethanol for several times, dried at 80 ℃ overnight, and calcined at 500 ℃ for 2 h in air to remove template and form MI-$TiO_2$. To enrich MI-$TiO_2$ with surface oxygen vacancies, the as-prepared samples were further mixed with appropriate mass of $NaBH_4$ by thorough grinding and calcined at specific temperature for 2 h under $N_2$ atmosphere. Finally, the cooled samples were washed with DI water to remove residual $NaBH_4$, which was denoted as MI-$TiO_{2-x}$. The effect of $NaBH_4$ dosage during MI-$TiO_{2-x}$ synthesis on its activity was preliminarily screened in a test (Fig. S1A). The optimum mass ratio of MI-$TiO_2$: $NaBH_4$ was determined as 1:7, and MI-$TiO_{2-x}$ shows the highest kinetic rate constant under this condition (Fig. S1B). Since decomposition products of excessive $NaBH_4$ would be coated onto the surface of calcined materials and inhibit the introduction of oxygen vacancy (as proved in Fig. S1C), a specific MI-$TiO_2$/$NaBH_4$ mass ratio of 1:7 was adopted to fabricate MI-$TiO_{2-x}$ in this case. Similarly, the calcination temperature was selected as 400 ℃ unless specified otherwise, since MI-$TiO_{2-x}$ exhibits the highest activity at this temperature (Fig. S2). For reference, pristine $TiO_2$ and oxygen vacancy engineered $TiO_2$ ($TiO_{2-x}$) were also prepared. Commercial Pd/C (3 wt%) and $Ti_4O_7$ powders were purchased as benchmarks. Electrodes were fabricated by dip-coating technology using carbon papers as substrates, and the details can be found in Text S2.

### 2.3. Electro-reductive dehalogenation of FLO

Electro-reductive dehalogenation of FLO was performed in a H-type electrochemical cell, with two-compartments (150 mL for each) and a Grion 0011 cation-exchange membrane to separate them. For a typical process, both compartments were filled with 100 mL $Na_2SO_4$ (50 mM) electrolyte, and a certain amount of FLO was added into catholyte to achieve an initial concentration of 10 mg $L^{-1}$. The initial pH is around 5.6 because FLO is naturally slightly acidic. A platinum foil (10 × 10 mm) and an Ag/AgCl (3.0 M KCl) serve as the counter and reference electrode, respectively. At intervals, 0.5 mL of cathodic solution was sampled and filtered with 0.45 μm PTFE membrane for further analysis.

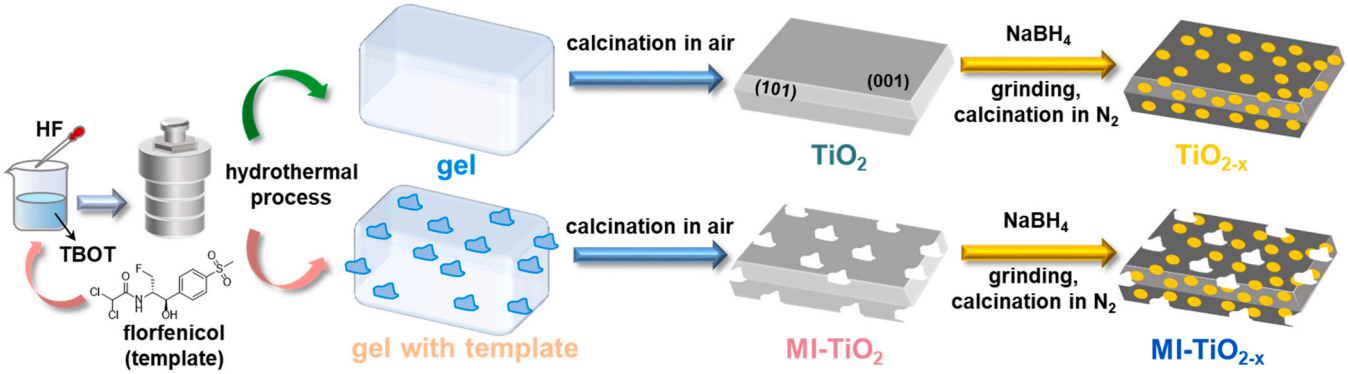


**Scheme 1.** Scheme for the synthesis of $TiO_2$, MI-$TiO_2$, $TiO_{2-x}$, and MI-$TiO_{2-x}$.

The cell was controlled by an electrochemical workstation (CHI 650D, Chenhua Co., China) at a constant driving bias. All the batch experiments were carried out in triplicate.

### 2.4. Characterizations and analytical methods

The technologies for morphological and structural characterizations of electrode materials are described in Text S3, including scanning electron microscope (SEM), high-resolution transmission electron microscope (HRTEM), energy dispersive X-ray spectroscopy (EDS), Fourier transform infrared spectroscopy (FTIR), X-ray diffraction (XRD), Raman spectra, and X-ray photoelectron spectroscopy (XPS). All the electrochemical characterizations involving cyclic voltammetry (CV), electrochemical capacitance, electrochemical impedance spectroscopy (EIS), and amperometric *I-t* (*I-t*) curve were performed by CHI 650D, using a glassy carbon (diameter=3 mm) coated with electrode materials as working electrode (Text S4). The concentration of FLO, and its dechlorinated intermediates including deschloro florfenicol (FLO−Cl) and dideschloro florfenicol (FLO−2Cl) were measured by a high-performance liquid chromatography (HPLC, LC-20AT, Shimadzu, Japan). Unquantified intermediates were analyzed using a LC-MS coupling system (Agilent 6210 TOF MS, Agilent, US). The released free chloride and fluoride were quantified by an ion chromatography (IC, Dionex-ICS2000, Thermo Fisher Scientific, US). All detailed analytical procedures can be found in Text S5.

### 2.5. DNA extraction, PCR amplification, and microbial community analysis

Microbial community genomic DNA was extracted from the corresponding sludge samples after 15-day incubation using the E.Z.N.A.® soil DNA Kit (Omega Bio-tek, Norcross, GA, U.S.) according to manufacturer's instructions. The details of DNA extraction and PCR amplification can be found in Text S6, and the processing of sequencing data can be found in Text S7.

### 2.6. Selected ARGs analysis by quantitative PCR

The major FLO resistance mechanism involves exportation of florfenicol by efflux pump coding genes [30]. Thus, *flo*R gene was selected in this study because it is a typical efflux pump gene [31]. The FLO-resistance genes amplified with primers pairs *flo*RF (5′-GAG GGTGTCGTCATCTACGG-3′) and *flo*RR (5′-GAGCATCGCCAGTATA GCCA-3′). All samples were run triplicates in the qPCR reactions. Gene copies of *flo*R were calculated from the standard curve.

## 3. Results and discussion

### 3.1. Structural and electrochemical characterizations of MI-$TiO_{2-x}$

The surface morphology of as-prepared MI-$TiO_{2-x}$ was firstly characterized by SEM, with $TiO_2$ as a reference. Compared with the standard $TiO_2$ nanosheets (Fig. S3A) [29], MI-$TiO_{2-x}$ features a disorganized surface (Fig. 1 A), because the removal of template molecules and the

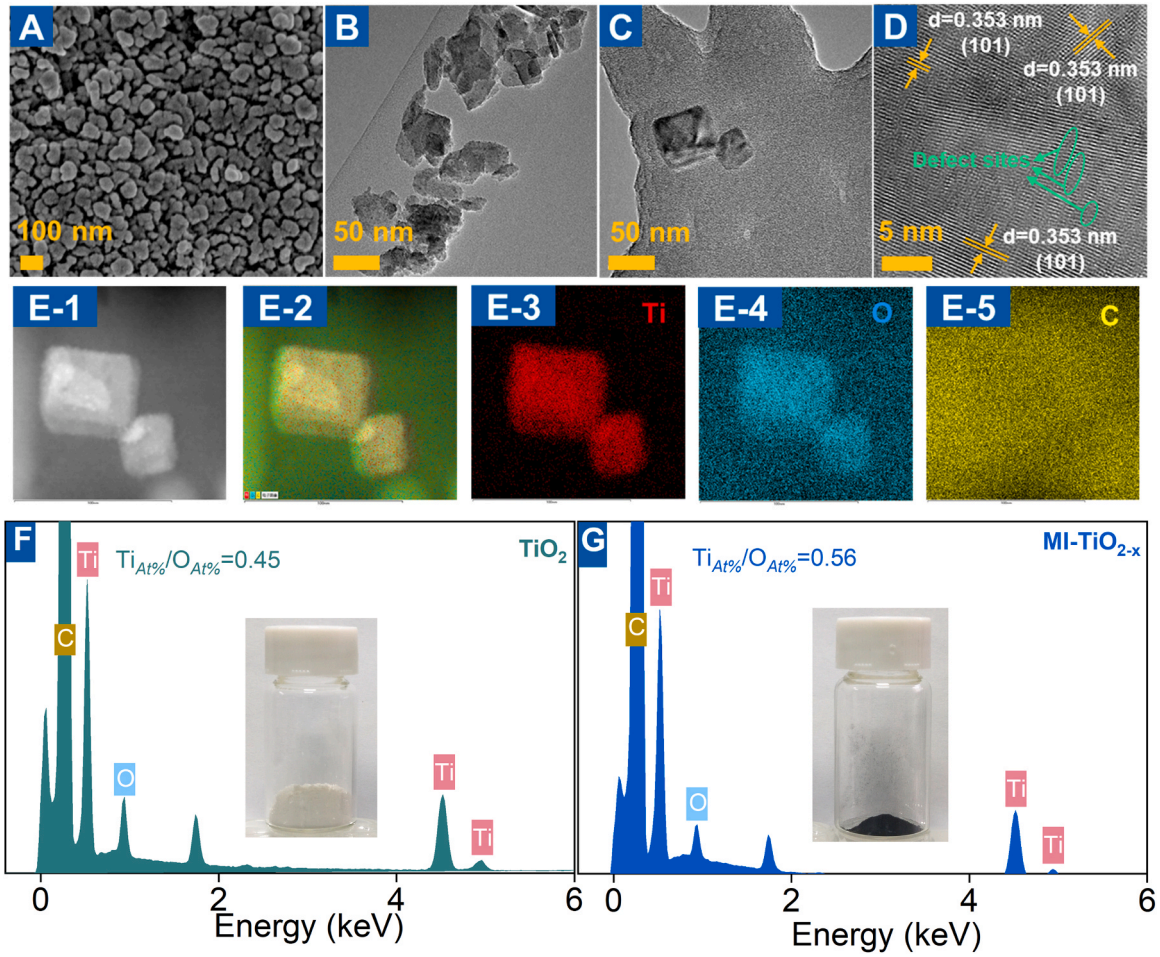


**Fig. 1.** (A) SEM, (B) lower magnification TEM, (C) higher magnification TEM, and (D) HRTEM images of MI-$TiO_{2-x}$, and (E-1 to E-5) elemental mapping; EDS spectra of (F) $TiO_2$ and (G) MI-$TiO_{2-x}$ (insets are the photographs of the samples).

introduction of oxygen vacancies (OVs) both lead to deformation from macroscopic view. The shape deformation has also been proved by the comparison between TEM images of MI-$TiO_{2-x}$ (Fig. 1B and C) and $TiO_2$ (Fig. S3B), since the outline of the rectangular sheets becomes irregular. In contrast with $TiO_2$ (Fig. S3C), not only the *d*-spacing of ~0.353 nm (corresponding to the {101} facet of anatase) but also the breakage of lattice fringes can be observed in the HRTEM image of MI-$TiO_{2-x}$ (Fig. 1D), which indicate the successful introduction of defect sites. The composition of MI-$TiO_{2-x}$ could be confirmed by the EDS maps, which mainly includes Ti and O elements with good distribution on the irregular nanosheets (Figs. 1E-1 to 1E-4). Besides this, the strong signals of C element on MI-$TiO_{2-x}$ sample (Fig. 1E-5) should be originated from the carbon conductive tape rather than the incomplete removal of FLO template, which is also observed on $TiO_2$ (Fig. S4). To track the fate of FLO template, FTIR spectra of FLO chemicals, gel with template, MI-$TiO_2$, and MI-$TiO_{2-x}$ during synthesis were all collected and compared. Fig. S5 suggests that gel with template inherits the peaks assigned to vibrations of C−F, C−Cl, aromatic C−H, C−N, −NH, C═O, and −CONH− from FLO chemicals, while all these peaks cannot be detected in both MI-$TiO_2$, and MI-$TiO_{2-x}$ samples. This result indicates the complete elimination of FLO template from MI-$TiO_{2-x}$ via calcination. Though there is no difference on elemental composition between $TiO_2$ (Fig. 1 F) and MI-$TiO_{2-x}$ (Fig. 1 G), the introduction of defect sites (as evidenced by EPR described later in this paper) has converted the appearance of samples from white to black (insets), which is in accordance with hydrogenated and self-doped $TiO_2$ [32].

The XRD pattern of MI-$TiO_{2-x}$ shows the reflection of synthetic anatase (PDF#86-1157, $Ti_{0.72}O_2$) and titanium monoxide (PDF#77-2170, TiO) phases, indicating that partial $TiO_2$ was reduced by overdosed $NaBH_4$ during the grinding and calcination (inside $N_2$ atmosphere) process (Fig. 2 A). Compared with $TiO_2$, MI-$TiO_2$ shows no remarkable changes on its XRD pattern, while that of $TiO_{2-x}$ features weakened characteristic peaks of anatase phase and occurrence of titanium monoxide phase. All these results suggest that the insertion and removal of template do not affect the crystal structure of the sample, while the $NaBH_4$ reduction may inevitably bring low-valent titania. The Raman spectra of samples were recorded to investigate the exerted influence of OVs on the geometric structure of $TiO_2$ (Fig. 2B). Apart from the unchanged three Raman modes assigned to $B_{1g}$ (394 $cm^{-1}$), $A_{1g}$ (514 $cm^{-1}$), and $E_g$ (635 $cm^{-1}$), the $E_g$ mode of both MI-$TiO_{2-x}$ and $TiO_{2-x}$ at 142 $cm^{-1}$ are positively shifted by 2.0 $cm^{-1}$, suggesting that most OVs related $Ti^{3+}$ should localize within the surface and subsurface of the sheets [33]. The results of full-scan XPS spectra shown in Fig. S6 again confirm the presence of Ti and O elements in MI-$TiO_{2-x}$, $TiO_{2-x}$, MI-$TiO_2$, and $TiO_2$. The high-resolution XPS spectra of Ti 2p show two peaks at around ~458.5 eV and ~464.4 eV in all samples (Fig. 2 C), corresponding to Ti $2p_{3/2}$ and Ti $2p_{1/2}$ spin-orbit doublets, respectively (which verifies the presence of $Ti^{4+}$) [34]. According to peak deconvolution, $NaBH_4$ reduction induces not only a slight shift on binding energies (~0.14 eV), but also distinct increase of $Ti^{3+}/Ti^{4+}$ peak area ratio in MI-$TiO_{2-x}$ and $TiO_{2-x}$ (Table S1), suggesting that more $Ti^{3+}$ is formed on the surface or subsurface of these samples. This is because OVs on surface or subsurface accompany $Ti^{3+}$ formation for charge compensation [35]. Fig. 2D illustrates the high-resolution O 1 s XPS spectra of all samples. Despite two de-convoluted peaks assigned to lattice oxygen (Ti-$O_{lattice}$) and surface hydroxyl oxygen (Ti-$OH_{surface}$) [36], oxygen species adsorbed on OVs can be observed in the spectra of MI-$TiO_{2-x}$ and $TiO_{2-x}$, which agrees with the results of HRTEM and Raman. All these

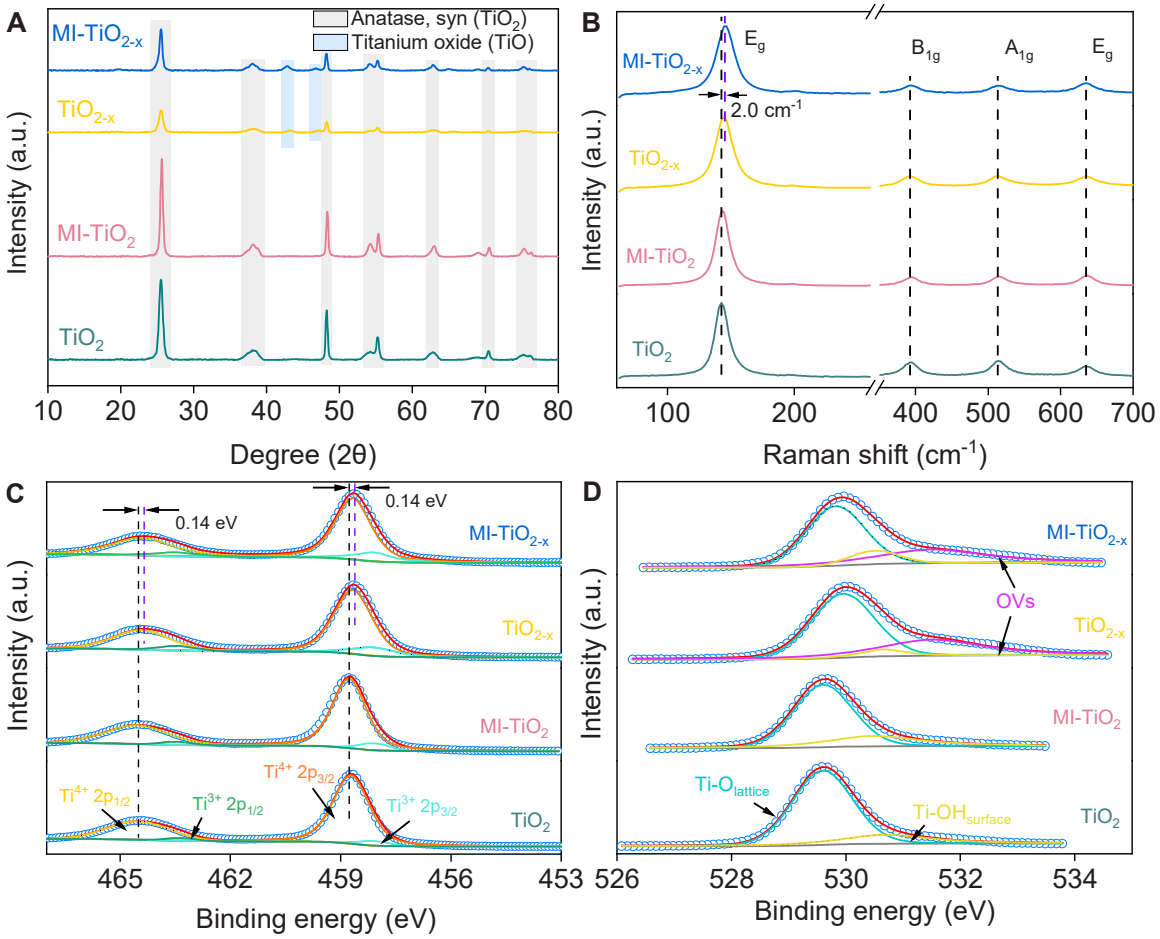


**Fig. 2.** (A) XRD patterns, (B) Raman spectra, and high-resolution XPS spectra of (C) Ti 2p and (D) O 1 s of $TiO_2$, MI-$TiO_2$, $TiO_{2-x}$, and MI-$TiO_{2-x}$.

evidences support the successful fabrication of MI-$TiO_{2-x}$.

Next, the redox reactions occurred on electrode materials were investigated using CV. By running CV scans within different potential windows (Fig. S7), several reductive (e.g. $O_2$ reduction, $Ti^{4+}$ reduction to $Ti^{3+}$, $H_2$ evolution) and oxidative (e.g. $H_2$ oxidation, $Ti^{3+}$ oxidation to $Ti^{4+}$) peaks are identified on different samples [37]. The CV curve of MI-$TiO_{2-x}$ shows no peak assigned to $O_2$ reduction and relative low activity for $H_2$ evolution, but apparent redox peaks belonging to $Ti^{4+}$ reduction to $Ti^{3+}$, and $Ti^{3+}$ oxidation to $Ti^{4+}$ (Fig. 3 A). Such mixed-valence Ti species cycling between + 3 and + 4 states at OV sites can act as an efficient redox electron shuttle and transport route for the migration of electrons [26,38]. The electrochemically active surface area (EASA) of all samples were estimated using the "capacitance" method [39]. By running a series of CV scans at different scan rates under a non-Faradic region (Fig. S8), the double layer capacitance ($C_{dl}$) can be obtained as the slope of charging current vs. scan rate (Text S8). The $C_{dl}$ of MI-$TiO_{2-x}$ (1.7 mF $cm^{-2}$) is nearly equal to that of MI-$TiO_2$ (1.4 mF $cm^{-2}$) and pristine $TiO_2$ (1.6 mF $cm^{-2}$), but is substantially lower than that of $TiO_{2-x}$ (4.0 mF $cm^{-2}$) (Fig. 3B). The lower EASA of MI-$TiO_{2-x}$ than that of $TiO_{2-x}$ is consistent with the variation trend of their specific surface area, since the EASA ratio (2.35) is close to the $S_{BET}$ ratio (2.17) (Fig. S9A). The formation of larger pores and cavities during the imprinting process of MI-$TiO_{2-x}$ should be responsible for this, as verified by its higher average pore diameter (19.5 nm) than that of $TiO_{2-x}$ (9.0 nm) (Fig. S9B). To further characterize the charge-transfer behavior of samples, their EIS spectra were recorded at a constant bias of − 1.2 V. The Nyquist plots of all samples exhibit a semicircle at high-frequency region and an almost vertical line at low-frequency region, which correspond to the interfacial charge transfer between electrode/electrolyte and mass transfer [10], respectively (Fig. 3 C). All the EIS data can be fitted well with the R(CR)W model by ZSimWin software (inset), which consists of bulk electrolyte solution resistance ($R_s$), electrical double layer capacitance ($C_d$), charge transfer resistance ($R_{ct}$), and Warburg impedance (W) [21]. In particular, the $R_{ct}$ of MI-$TiO_{2-x}$ (10.02 Ω $cm^2$), $TiO_{2-x}$ (10.03 Ω $cm^2$), and MI-$TiO_2$ (10.24 Ω $cm^2$) are similar, which accounts for 83–85 % of that of $TiO_2$ (Table S2). This result suggests that not only OVs, but also MI sites enhances the interfacial charge transfer kinetics of $TiO_2$. This is because the fabrication of MI sites by impregnating FLO template during the hydrolysis of tetrabutyl titanate may inevitably introduce defects, as evidenced by the $Ti^{3+}$ on surface or subsurface (Fig. 2 C). To examine the activity of these samples, the amperometric *I-t* curves were performed on samples with carbon paper as substrates, at a constant bias of − 1.2 V and initial FLO concentration of 10 mg $L^{-1}$. Fig. 3D suggests that the response current of all samples undergoes rapid decrease at the initial stage and eventually reaches a steady state, probably due to the double-layer discharge. In detail, the reduction current of FLO on MI-$TiO_{2-x}$ is always higher than that on other samples, implying that more FLO can be reduced on MI-$TiO_{2-x}$.

### 3.2. *Electro-reductive performance of MI-$TiO_{2-x}$ for FLO*

The comparison on electro-reductive dehalogenation activity of electrode materials for FLO is presented in Fig. S10. The fitted results of

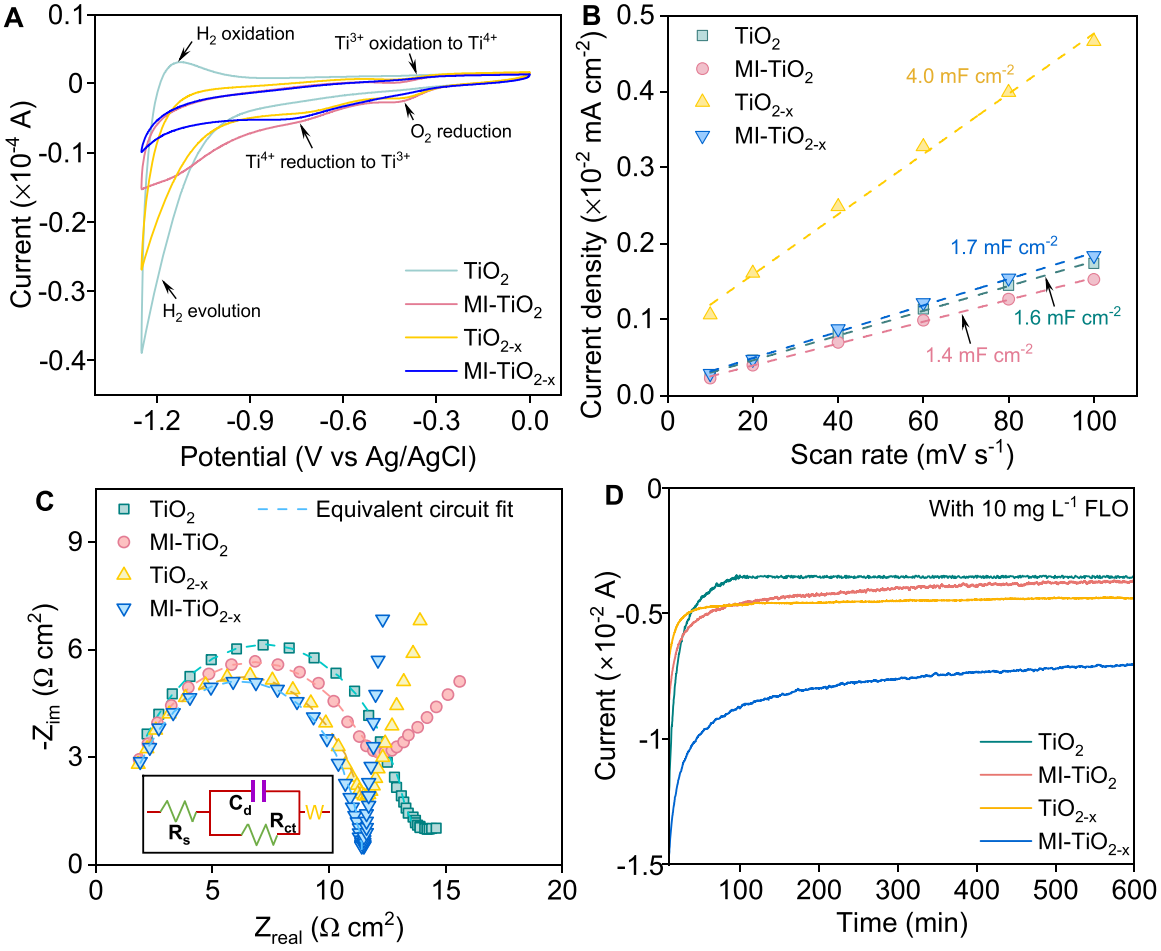


**Fig. 3.** (A) CV scans within the potential window of − 1.25 V to 0 V at 100 mV $s^{-1}$, (B) plots of capacitive current density as a function of scan rate, and (C) Nyquist plots of $TiO_2$, MI-$TiO_2$, $TiO_{2-x}$, and MI-$TiO_{2-x}$ coated on glassy carbon, and (D) the amperometric *I*-t curves of these samples with carbon paper as substrates, at a constant bias of − 1.2 V and initial FLO concentration of 10 mg $L^{-1}$ (test condition: [$Na_2SO_4$] = 50 mM).

pseudo-first-order kinetic model (Fig. 4 A) suggest that MI-$TiO_{2-x}$ could degrade 97.9 % FLO within 180 min with a $k_{obs,\ FLO}$ of 0.021 $min^{-1}$, which is higher than not only $TiO_{2-x}$ (0.013 $min^{-1}$), MI-$TiO_2$ (0.011 $min^{-1}$), and $TiO_2$ (0.009 $min^{-1}$), but also the commercial Pd/C (0.019 $min^{-1}$) and $Ti_4O_7$ (0.007 $min^{-1}$). To accurately evaluate the activity of these materials, their $k_{obs,\ FLO}$ were normalized with their loadings. As suggested by Table S3, MI-$TiO_{2-x}$ shows higher $k_{obs,\ FLO}$/loading value than most of the recent electrocatalysts. Hence, MI-$TiO_{2-x}$ exhibits a potential to be an alternative for the abatement of aqueous FLO due to its high reactivity. The impact of applied bias on FLO removal was then investigated (Fig. S11), since the control of electrode potential is the key to manipulate an electrochemical reaction. Fig. 4B suggests that the $k_{obs,\ FLO}$ could be monotonously enhanced by intensifying the applied bias (from −0.8 to −1.2 V), in terms of providing more powerful driving force. But excessively increasing the cathodic potential (i.e. −1.4 V) would trigger serious hydrogen evolution reaction (HER) and thereby suppressing the dehalogenation activity [40]. The effect of solution pH was also studied (Fig. S12), because it is the core water chemical factor to regulate the competition between electro-reductive dehalogenation and HER [41]. Fig. 4 C shows that MI-$TiO_{2-x}$ under the weak acidic environment with initial pH 5.65 (due to the dissolution of FLO) displays higher $k_{obs,\ FLO}$ (0.021 $min^{-1}$) than that under acidic (0.016 $min^{-1}$, initial pH 3.56) and alkaline (0.011 $min^{-1}$, pH 10.06) conditions. Though lower pH offers more $H^+$ to boost the dehalogenation via both direct cathodic reduction and atomic H*, too fast HER under strong acidic condition would outcompete dehalogenation, by producing $H_2$ bubbles to inhibit the mass transfer of targeted contaminants onto the surface of catalyst [42]. According to the remarkably lower removal efficiency of FLO at pH 10.06 (83.8 % within 180 min, Fig. S12), it is more competitive to operate MI-$TiO_{2-x}$ at weak acidic and neutral conditions, rather than alkaline medium.

The reusability of MI-$TiO_{2-x}$ was probed by 9 consecutive runs. As shown in Fig. 4D, MI-$TiO_{2-x}$ demonstrates high removal efficiency (> 95.0 %) for FLO in each run, albeit continuously slower as suggested by the fitted $k_{obs,\ FLO}$ (Fig. S13). The gradual decreasing $k_{obs,\ FLO}$ is probably attributed to the adsorption of dehalogenated products, which can be restored by soaking the used MI-$TiO_{2-x}$ electrode into pure methanol for a few seconds. To study the possible dissolution of electrode materials, samples of catholyte after each cycle were digested with *aqua regia* and detected by ICP-OES. As recorded in Table S4, the released Ti after each run is less than 0.003 mg and the sum of Ti loss only accounts for 0.27 % of the original loading (Text S2). Actually, the featured double peaks included in XPS spectra of Ti 2p belonging to used MI-$TiO_{2-x}$ shows no binding energy shift when compared to the newly prepared one (Fig. S14), reflecting the robustness of MI-$TiO_{2-x}$.

Pd/C is a common benchmark when performing the electrochemical reductive dehalogenation of halogenated environmental pollutants [43], but inevitably suffers from rapid deactivation when exposed to bicarbonate ($HCO_3^-$) and sulfur species ($S^{2-}$ or $SO_3^{2-}$) [44]. Fig. 4E and F present the removal of FLO in the presence of several solutes by MI-$TiO_{2-x}$ and Pd/C, respectively. Overall, the negative effect of humic acid (HA), $Cl^-$, and $HCO_3^-$ on FLO removal could be neglected for both electrode materials. In contrast, presence of $SO_3^{2-}$ and $S^{2-}$ species largely reduce the electro-reductive activity of Pd/C, presumably caused by

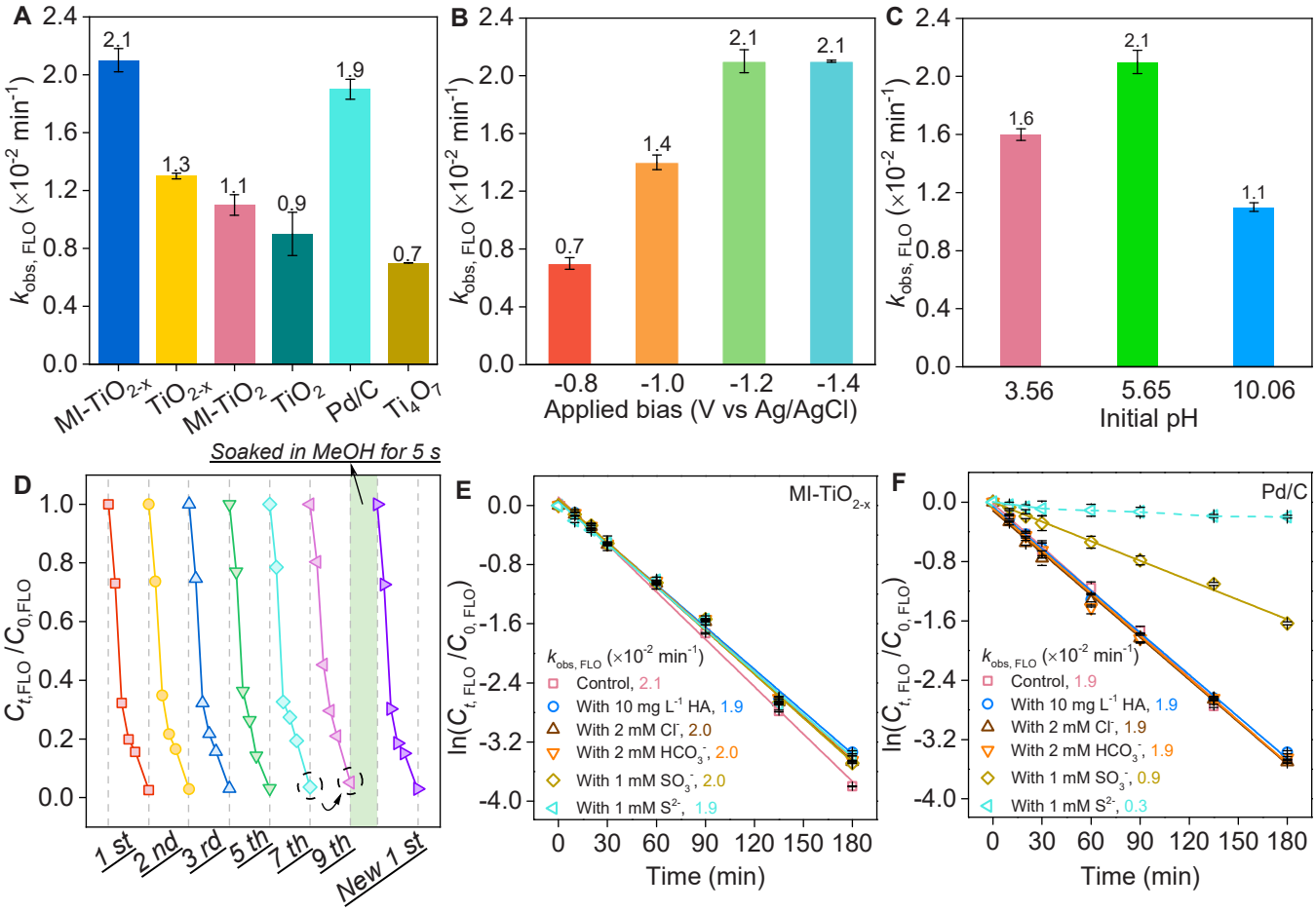


**Fig. 4.** (A) Pseudo-first-order kinetic rate constants of FLO removal ($k_{obs,\ FLO}$) by different electrode materials; Effect of (B) applied bias and (C) initial pH on $k_{obs,\ FLO}$ by MI-$TiO_{2-x}$; (D) Evolution of $C_{t,\ FLO}/C_{0,\ FLO}$ in each run during a consecutive 10-run reusability test of MI-$TiO_{2-x}$; Effect of coexisting HA (10 mg $L^{-1}$), $Cl^-$ (2 mM), $HCO_3^-$ (2 mM), $SO_3^{2-}$ (1 mM), and $S^{2-}$ (1 mM) on $k_{obs,\ FLO}$ by (E) MI-$TiO_{2-x}$ and (F) Pd/C (reaction condition: $[FLO]_0$ = 10 mg $L^{-1}$, $[Na_2SO_4]$= 50 mM).

their chemisorption to active sites and thus forming Pd-S compounds [15]. Compared with Pd/C, MI-$TiO_{2-x}$ shows high anti-fouling property for conventional coexisting components, which is anticipated to achieve good performance for dehalogenating FLO in waste streams.

Lastly, additional representative antibiotics involving nitrofurazone, furazolidone, metronidazole, chloramphenicol, and thiamphenicol were tested by MI-$TiO_{2-x}$. Fig. S15A indicates that more than 80 % of all these antibiotics (10 mg $L^{-1}$) can be removed within 240 min at − 1.2 V, though MI-$TiO_{2-x}$ features different activities for them (Fig. S15B). This difference may be originated from the diverse molecular structures of these antibiotics [9]. More importantly, MI sites ensures the preference for FLO removal by MI-$TiO_{2-x}$, which would be discussed in Section *3.4*.

### *3.3. Dehalogenation mechanism of FLO over MI-$TiO_{2-x}$*

Both direct electron transfer (DET) and indirect reduction via H* have been identified in a typical electro-reductive dehalogenation system [11]. To distinguish their contributions in this case, quenching tests with increasing levels of *tert*-butanol (TBA, considered as the scavenger for H*) were first performed (Fig. S16). Fig. 5 A suggests that TBA can largely reduce the $k_{obs,\ FLO}$, but the FLO removal at 180 min with presence of overdose TBA (FLO/TBA=1:10) accounts for 88.8 % of the pristine group. That is to say, DET rather than H*-mediated indirect route dominates the dehalogenation of FLO by MI-$TiO_{2-x}$. To get insight into the dehalogenation mechanism, CV tests were then performed over MI-$TiO_{2-x}$ in the presence of FLO with different scan rates (Fig. S17A). One prominent reduction peak assigned to FLO reduction can be found on CV curves of both electrodes. The reduction peak current ($I_p$) is found proportional to $v^{1/2}$ (Fig. 5B), suggesting that the cathodic reduction process is kinetically limited by diffusion of FLO from bulk catholyte to the electrode surface. Concomitantly, the negative shifted reduction peak potential ($E_p$) can be correlated well with increasing $v^{1/2}$. These phenomena can be attributed to the joint control of mass transfer and electron transfer during the voltammetric reduction of FLO over MI-$TiO_{2-x}$ [45]. Generally, DET induced reductive cleavage of carbon-halogen bond may proceed through stepwise or concerted mechanism, meaning that the electron transfer and bond rupture may occur in sequence or take place simultaneously [46]. To further interpret the dehalogenation mechanism of FLO over MI-$TiO_{2-x}$, a diagnostic parameter $k$ was calculated according to the slope of the linear variation of $E_p$ as a function of log($v$) (described in Text S9). A $k$ value of 0.44 presented in Fig. S17B indicates that the reductive dehalogenation of FLO over MI-$TiO_{2-x}$ obeys a stepwise mechanism (which refers to a $k$ lying between 0.4 and 0.5), and the electron transfer rather than the carbon-halogen bond breakage should be the rate determining step [47]. This result highlights the importance of enhancing the electron transfer process from electrode materials to FLO, which fundamentally promotes the electro-reductive activity of MI-$TiO_{2-x}$.

Dechlorination is considered as the only step during the electro-reductive dehalogenation by Pd and $MoS_2$ modified electrodes, which gives dechlorinated FLO−Cl and FLO− 2Cl as products [12,45]. To study the product distribution during FLO removal by MI-$TiO_{2-x}$,

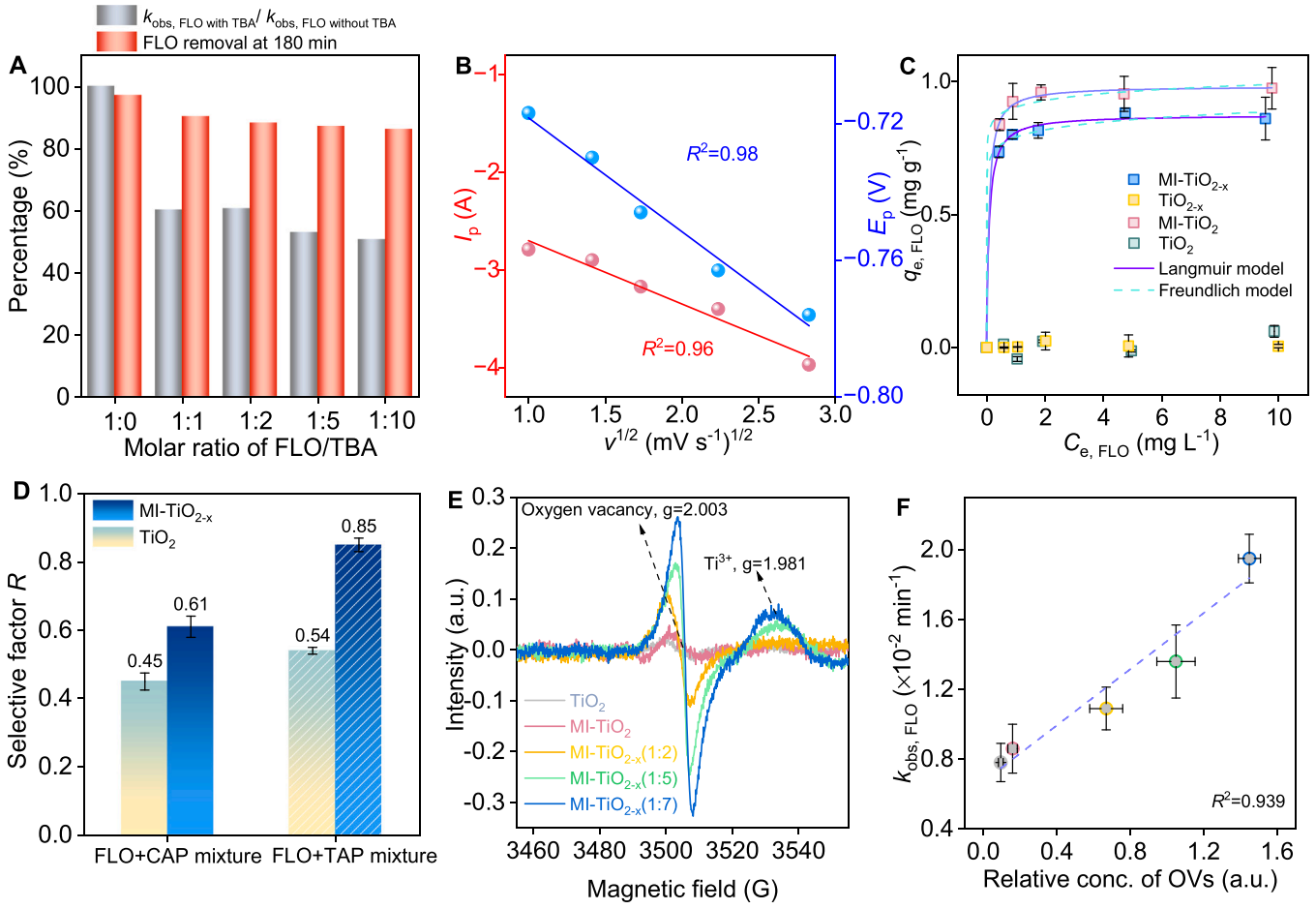


**Fig. 5.** (A) Impact of TBA on $k_{obs,\ FLO}$ and FLO removal at 180 min by MI-$TiO_{2-x}$; (B) Plots of reduction peak current, and cathodic peak potential of FLO over MI-$TiO_{2-x}$, as a function of $v^{1/2}$ (scan rate) inside 50 mM air-free phosphate buffer solution; (C) Adsorption isotherms recorded for FLO onto $TiO_2$, MI-$TiO_2$, $TiO_{2-x}$, and MI-$TiO_{2-x}$; (D) Anti-interference test on MI-$TiO_{2-x}$ towards 10 mg $L^{-1}$ FLO, in the presence of 10 mg $L^{-1}$ CAP or TAP; (E) EPR spectra of a group of MI-$TiO_{2-x}$ with increasing OVs, which was fabricated by adding increasing mass ratio of $NaBH_4$; (F) Correlation between $k_{obs,\ FLO}$ and relative concentration of OVs belonging to MI-$TiO_{2-x}$.

batches with different initial FLO concentration levels were performed (Fig. S18A1, B1, C1, and D1). By summarizing the carbon fraction (denoted as moles of quantified product at time $t$ versus moles of FLO at time 0) of each chemical, the unbalance of carbon mass can be observed in all batches, validating the generation of unquantified products. Moreover, the fitted $k_{obs,\ FLO}$ is negatively correlated with the initial FLO concentration (Fig. S19), indicating that the performance of MI-$TiO_{2-x}$ for FLO abatement is limited by mass transfer. Even at low concentration level (1 mg $L^{-1}$, Fig. S18D1), MI-$TiO_{2-x}$ still enables 90.7 % FLO removal within 240 min, while complete removal can be expected by prolonging reaction time. The detection on free $F^-$ during FLO removal indicates the occurrence of defluorination step. For batches with $[FLO]_0$ at 10 and 5 mg $L^{-1}$ (Fig. S18A2and B2), deep dechlorination (>97.5 %) and high defluorination (>65.7 %) can be achieved within 180 min, which validate the strong catalytic activity of MI-$TiO_{2-x}$. Even if $[FLO]_0$ is reduced to 2 and 1 mg $L^{-1}$, MI-$TiO_{2-x}$ still show acceptable dehalogenation efficiency for these batches (Fig. S18C2and D2), which corresponds to their FLO removal (Fig. S18C1and D1). Similar defluorination behavior of FLO has been reported by employing a cathode material of Fe-doped CoP nanotubes array, which leads to extra defluorinated intermediates like FLO−F, FLO−Cl−F and FLO− 2Cl−F [48]. Considering the lack of standard chemicals of defluorinated intermediates, the Faradic efficiency (FE) of all batches could be determined by calculating the electrons required for carbon-halogen bond dissociation versus the input electric quantity during electro-reductive dehalogenation of FLO (described in Text S10). Based on the measurement of released free $Cl^-$ and $F^-$, and the recorded electric quantity (Fig. S20), FE less than 5 % can be obtained for all batches (Fig. S18A2, B2, C2 and D2) due to the competition of ubiquitous HER, which leaves room for improvement.

The LC-MS analysis was also performed to systematically track the possible products during FLO removal. Table S5 summarizes the recognized molecules from both the representative LC profile and mass spectra (Fig. S21), which involves above-mentioned FLO−Cl, FLO− 2Cl, FLO−F, FLO−Cl−F, and FLO− 2Cl−F. The LC peak area of all molecules was plotted as a function of reaction time to semi-quantitatively describe the product evolution (Fig. S22A). Specifically, the signals assigned to FLO−Cl, FLO− 2Cl, FLO−F, and FLO−Cl−F firstly increase and then decrease as the reaction proceeds, while that of FLO− 2Cl−F is continuously rising. Therefore, FLO would successively experience dechlorination/defluorination in a step-by-step manner and finally converted into FLO− 2Cl−F (Fig. S22B).

### 3.4. Insights into role of MI sites and OVs

To elucidate the role of MI sites over MI-$TiO_{2-x}$, isotherm experiments were firstly performed by a batch equilibration method. The vials filled with FLO solution and electrode materials were placed on a shaker and agitated in dark for 72 h to reach equilibrium. The adsorption isotherm plots of FLO onto MI-$TiO_{2-x}$, MI-$TiO_2$, $TiO_{2-x}$, and $TiO_2$ are depicted in Fig. 5 C, and their corresponding regression parameters by the Langmuir and Freundlich models are listed in Table S6. Only MI-$TiO_{2-x}$ and MI-$TiO_2$ show adsorption ability for FLO, while the adsorption behavior of FLO onto $TiO_{2-x}$, and $TiO_2$ is negligible. The isotherms of MI-$TiO_{2-x}$ and MI-$TiO_2$ were fitted better by the Langmuir model than by the Freundlich model, suggesting that the adsorption of FLO onto these materials tends toward monolayer but not multilayer. The calculated adsorption capacity ($q_m$) of FLO onto MI-$TiO_2$ (0.983 mg $g^{-1}$) is indeed higher than that onto MI-$TiO_{2-x}$ (0.875 mg $g^{-1}$), meaning that the number of MI sites on MI-$TiO_2$ is slightly more than that on MI-$TiO_{2-x}$. This is probably because the introduction of OVs on surface or subsurface would occupy some original MI sites on MI-$TiO_2$. Combining these results with the enhanced activity shown in Section 3.2, MI sites are certified to boost the mass transfer of FLO from the bulk solution to the surface of electrode, and thus contributing to faster dehalogenation kinetics.

To unveil the recognition capability of MI sites over MI-$TiO_{2-x}$, designed anti-interference tests were performed in a combined pollution system. The FLO removal batch by MI-$TiO_{2-x}$ was operated in the presence of chloramphenicol (CAP) or thiamphenicol (TAP), respectively, which are known as the analogues of FLO (Fig. S23A). On the whole, MI-$TiO_{2-x}$ displays higher removal rate for FLO than CAP or TAP (Fig. S23B and D), while pristine $TiO_2$ fails to show any preference in the binary combined pollution system (Fig. S23C and E). A selective factor $R$, which is defined as $R = k_{obs,\ FLO}/(k_{obs,\ FLO} + k_{obs,\ coexisting\ chemical})$, can quantitatively describe the selective removal of FLO by MI-$TiO_{2-x}$. Fig. 5D indicates that $R$ belonging to MI-$TiO_{2-x}$ is 35.6 % and 57.4 % higher than that of $TiO_2$ under the interference of CAP and TAP, respectively, emphasizing that MI-$TiO_{2-x}$ preferentially dehalogenates FLO even in competition with similar structural molecules. Such observation suggests that construction of MI sites also endows MI-$TiO_{2-x}$ with strong selectivity.

The building of surface OVs over $TiO_2$ catalyst is deemed to increase the electric conductivity and reduce the charge transfer resistance, and thus resulting in good electrocatalytic activity [26]. The results illustrated in Section 3.2. simply interpret the enhanced FLO removal by oxygen vacancy engineered $TiO_2$, but the quantitative analysis is lacked. To explore the relationship between the concentration of OVs and the dehalogenation activity, electron paramagnetic resonance (EPR) was performed on a group of MI-$TiO_{2-x}$ fabricated by increasing mass ratio of $NaBH_4$ (whose dehalogenation kinetics for FLO have been collected as Fig. S1). Signals of OVs and accompanied $Ti^{3+}$ species with g factors of 2.003 and 1.981 could both be detected in all spectra (Fig. 5E). To represent the relative concentration of OVs, their peak areas were obtained by integration (Fig. S24). By plotting the $k_{obs,\ FLO}$ of these electrode materials (derived from Fig. S1) with their relative concentration of OVs, a good linear correlation is uncovered, demonstrating that creation of OVs over MI-$TiO_{2-x}$ drives its accelerated dehalogenation performance for FLO, by means of improving the electrode/solution interfacial electron transfer.

### 3.5. Preferential remediation of FLO and elimination of ARGs in swine wastewater

To test whether MI-$TiO_{2-x}$ can keep its dehalogenation activity in actual aqueous matrices, and whether electro-reductive dehalogenation can lead to AGRs elimination in subsequent receiving unit, an electro-reductive and biological coupling system was set up (Fig. 6 A). The simulated influent of such system was sampled from the tailwater of a swine farm located in Hangzhou, and was spiked with 2 mg $L^{-1}$ FLO and pre-incubated for 5 d. On the basis of DB3301/T 1046-2014 (Discharge standard of pollutants for livestock and poultry breeding, Hangzhou), the tailwater of this swine farm should have been discharged into the municipal wastewater treatment plant via sewerage system (Fig. S25). To mimic the scenario, the activated sludge included in the biological treatment unit in the coupling system was sourced from a pilot-scale aerobic continuous reactor in municipal wastewater treatment plant, which had been operating for domestic sewage treatment for two years at the time of sampling. The appearance and physicochemical property of both the tailwater and sludge were given in Fig. S26 and Table S7.

#### 3.5.1. FLO removal in swine wastewater

Fig. 6B depicts the comparison on FLO removal from simulated influent by MI-$TiO_{2-x}$ and Pd/C. Although the $k_{obs,\ FLO}$ of MI-$TiO_{2-x}$ suffers an 80 % loss when compared to that of itself in pure 50 mM $Na_2SO_4$ (Fig. 4 A), more than 90 % of FLO can be removed by prolonging reaction time to 8 h. In detail, the $k_{obs,\ FLO}$ of MI-$TiO_{2-x}$ outperforms that of Pd/C, and the gap between them becomes wider by contrast with their performance in 50 mM $Na_2SO_4$ (Fig. 4 A). This result proves that MI-$TiO_{2-x}$ is more competitive to dehalogenate FLO in swine wastewater, while Pd/C may be more susceptible to deactivation over time (e.g. by reduced S species come from the microbial reduction of $SO_4^{2-}$). Collectively, electro-reductive dehalogenation by MI-$TiO_{2-x}$ for removal of

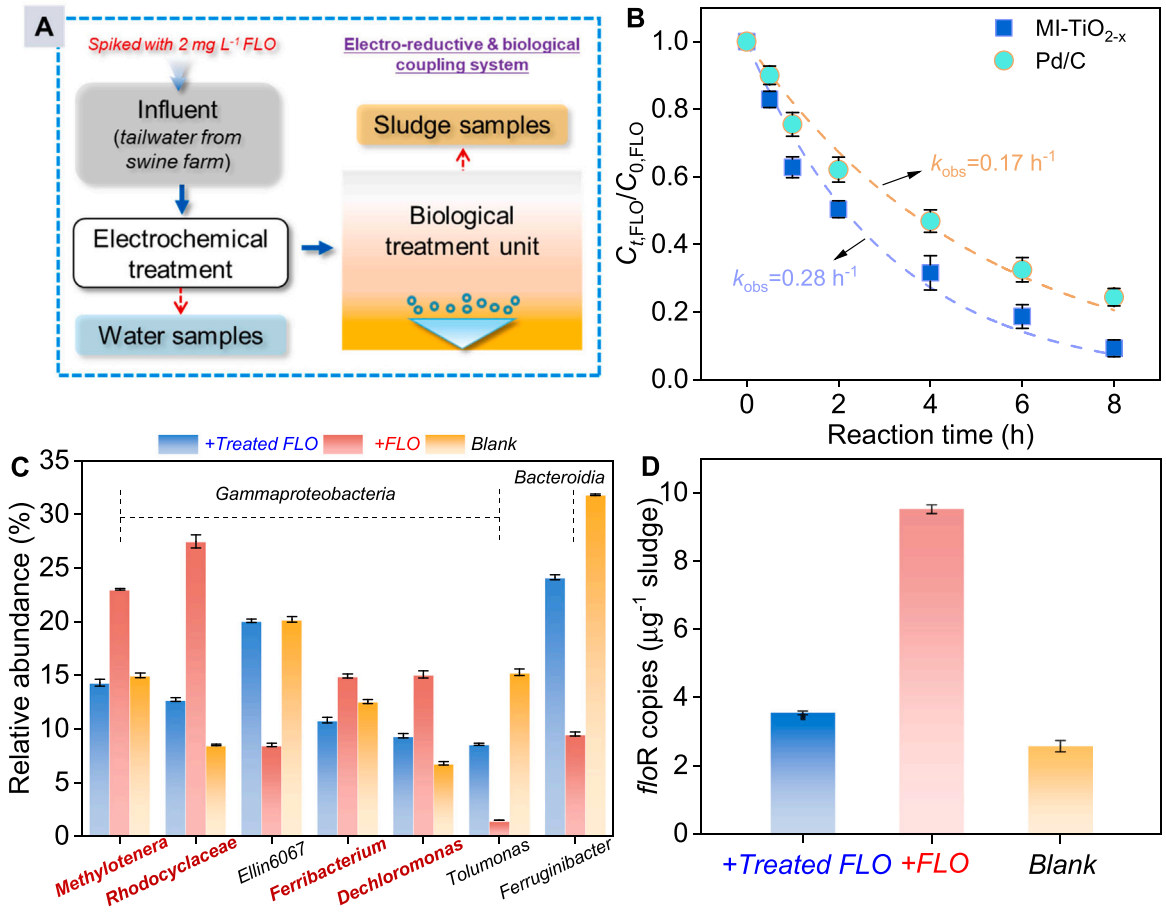


**Fig. 6.** (A) Schematic illustration of the electro-reductive and biological coupling system; (B) Decontamination of FLO-contaminated swine wastewater by MI-$TiO_{2-x}$ and Pd/C; (C) Relative abundance of predominant microbial community at genus level (top 7 genera), and (D) abundance of *flo*R in sludge samples.

low-content FLO from swine wastewater is feasible.

### 3.5.2. *ARGs elimination in biological treatment unit*

The subsequent effect on microbial community succession and abundance of *flo*R in receiving unit caused by dehalogenation of FLO were explored. More precisely, FLO-contaminated swine wastewater with electro-reductive dehalogenation by MI-$TiO_{2-x}$ for 8 h was added into the biological treatment unit and incubated for 15 d, and sludge sample was collected for analysis (denoted as +treated FLO batch). As references, sludge sample from a parallel unit with FLO-contaminated swine wastewater for 15-day pre-incubation (denoted as +FLO batch), and virgin sludge sample with non-contaminated swine wastewater (denoted as blank batch) were also performed.

Under FLO stress, the relative abundance of most bacteria phyla in +FLO batch declines when compared to the blank, except for *Proteobacteria* and *Actinobacteriota*, which increases from 39.8 % to 45.0 %, and 4.9 % to 7.4 %, respectively (Fig. S27). Generally, *Proteobacteria* and *Actinobacteriota* are often associated with the degradation of antibiotics, and reported as the main potential hosts of ARGs [49,50]. It's worth noting that the microbial community composition of +treated FLO and blank batches are consistent with each other, reflecting that dehalogenation of FLO by MI-$TiO_{2-x}$ for 8 h radically gets rid of the antibacterial activity of FLO. Fig. 6 C lists the relative abundance of the predominant genera (top 7) in each batch at genus level, among which *Methylotenera*, *Rhodocyclaceae*, *Ferribacterium*, and *Dechloromonas* are more enriched in +FLO batch than in the blank, even though under FLO stress. Such phenomenon could be linked to the functions of these bacteria, since *Methylotenera* and *Rhodocyclaceae* are potential degrader for benzene homologues [51,52], and *Ferribacterium* can assimilate carbon from benzene [53], and *Dechloromonas* has been involved in dechlorination/mineralization of chlorinated aromatics like 2,4-dichlorophenol [54]. As for +treated FLO batch, dehalogenation of FLO is conducive to favoring the further bio-mineralization of benzene-structured products, which should be responsible for the reduction of these genera. At last, PCoA and the Bray-Curtis distance again proves the similarity between +treated FLO and blank batches (Fig. S28, $R^2 = 0.65$, $p < 0.05$, *adonis*), indicating that microbial community succession is regulated by dehalogenating FLO.

The abundance of *flo*R in +treated FLO batch only accounts for 37.5 % of that in +FLO batch, and is 1.38-fold higher than that of the blank (Fig. 6D). To be specific, the *flo*R in +FLO batch may come from the addition of FLO-contaminated swine wastewater, and the proliferation under stimulation of FLO. Accordingly, the *flo*R elimination in +treated FLO batch may stem from I) the direct destruction of ARGs by destroying their host cells by electro-reductive treatment (addressed in Text S11), and II) the prevention of ARGs proliferation by dehalogenating FLO.

## 4. Conclusion

In this work, a noble metal-free MI-$TiO_{2-x}$ cathode material was customized to preferentially decontaminate low-content halogenated antibiotics from complex water matrices in the presence of high-concentration interferents, as well as eliminating ARGs. MI-$TiO_{2-x}$ outcompetes pristine/modified $TiO_2$, commercial Pd/C and $Ti_4O_7$ for FLO removal, and sustains its high efficiency/stability within a wide pH window, or with coexisting solutes. Deep dehalogenation of FLO can be achieved over MI-$TiO_{2-x}$ in a step-by-step manner. MI sites enhances the mass transfer of FLO towards MI-$TiO_{2-x}$ and endows the process with

strong selectivity, while OVs facilitates interfacial charge transfer. In a batch mode, MI-$TiO_{2-x}$ smoothly removes trace FLO from swine wastewater and therefore simultaneously impacting microbial community succession in receiving biological treatment unit, and eliminating ARGs. The findings in this study shed light on the advantage of remediating low-concentration antibiotic-contaminated wastewater with electro-reductive dehalogenation.

## CRediT authorship contribution statement

**Zimo Lou:** Conceptualization, Investigation, Funding acquisition, Writing – original draft. **Xiaofei Wen:** Conceptualization, Methodology, Data curation. **Ludi Song:** Data curation, Formal analysis. **Chen Yan:** Validation, Investigation. **Hongxu Chen:** Software, Formal analysis. **Tao Lu:** Methodology, Writing – review & editing. **Jianming Yu:** Funding acquisition, Writing - review & editing. **Xinhua Xu:** Funding acquisition, Writing - review & editing. **Jiansheng Li:** Supervision, Funding acquisition, Writing - review & editing.

## Declaration of Competing Interest

The authors declare that they have no known competing financial interests or personal relationships that could have appeared to influence the work reported in this paper.

## Data availability

Data will be made available on request.

## Acknowledgements

This work was supported by the National Natural Science Foundation of China (22006132, 22276096), the Zhejiang Provincial Natural Science Foundation of China (LQ21B070002), the National Key Research and Development Program of China (2022YFC3203403), and the Key Research and Development Program of Zhejiang Province (2020C03085).

## Appendix A. Supporting information

Supplementary data associated with this article can be found in the online version at doi:10.1016/j.apcatb.2023.122923.

## References

[1] D.G.J. Larsson, C.-F. Flach, Antibiotic resistance in the environment, Nat. Rev. Microbiol. 20 (2022) 257–269, https://doi.org/10.1038/s41579-021-00649-x.
[2] N.H. Tran, M. Reinhard, K.Y.H. Gin, Occurrence and fate of emerging contaminants in municipal wastewater treatment plants from different geographical regions-a review, Water Res. 133 (2018) 182–207, https://doi.org/10.1016/j.watres.2017.12.029.
[3] A.S. Oberoi, Y. Jia, H. Zhang, S.K. Khanal, H. Lu, Insights into the fate and removal of antibiotics in engineered biological treatment systems: a critical review, Environ. Sci. Technol. 53 (2019) 7234–7264, https://doi.org/10.1021/acs.est.9b01131.
[4] A. Pruden, R. Pei, H. Storteboom, K.H. Carlson, Antibiotic resistance genes as emerging contaminants: studies in Northern Colorado, Environ. Sci. Technol. 40 (2006) 7445–7450, https://doi.org/10.1021/es060413l.
[5] B. Liang, H. Cheng, D. Kong, S.H. Gao, F. Sun, D. Cui, F. Kong, A. Zhou, W. Liu, N. Ren, W. Wu, A. Wang, D.J. Lee, Accelerated reduction of chlorinated nitroaromatic antibiotic chloramphenicol by biocathode, Environ. Sci. Technol. 47 (2013) 5353–5361, https://doi.org/10.1021/es400933h.
[6] M. Harza, H. Joshi, J.B. Williams, J.E.M. Watts, Antibiotics and antibiotic resistant bacteria/genes in urban wastewater: a comparison of their fate in conventional treatment systems and constructed wetlands, Chemosphere 303 (2022), 135148, https://doi.org/10.1016/j.chemosphere.2022.135148.
[7] S. Rodriguez-Mozaz, S. Chamorro, E. Marti, B. Huerta, M. Gros, A. Sànchez-Melsió, C.M. Borrego, D. Barceló, J.L. Balcázar, Occurrence of antibiotics and antibiotic resistance genes in hospital and urban wastewaters and their impact on the receiving river, Water Res. 69 (2015) 234–242, https://doi.org/10.1016/j.watres.2014.11.021.
[8] D. Henschler, Toxicity of chlorinated organic compounds: effects of the introduction of chlorine in organic molecules, Angew. Chem. Int. Ed. 33 (1994) 1920–1935, https://doi.org/10.1002/anie.199419201.
[9] D. Kong, B. Liang, H. Yun, H. Cheng, J. Ma, M. Cui, A. Wang, N. Ren, Cathodic degradation of antibiotics: characterization and pathway analysis, Water Res. 72 (2015) 281–292, https://doi.org/10.1016/j.watres.2015.01.025.
[10] L. Yang, Z. Chen, T. Ma, S. Zhang, W. Dai, X. Xiao, X. Lou, J. Zou, X. Tu, L. Yang, S. Luo, Efficient electrochemical dehalogenation of florfenicol without discharging toxic intermediates via direct electron transfer over electrochromic $WO_3$, Chem. Eng. J. 412 (2021), 127481, https://doi.org/10.1016/j.cej.2020.127481.
[11] H. Liu, J. Han, J. Yuan, C. Liu, D. Wang, T. Liu, M. Liu, J. Luo, A. Wang, J. C. Crittenden, Deep dehalogenation of florfenicol using crystalline CoP nanosheet arrays on a Ti plate via direct cathodic reduction and atomic H, Environ. Sci. Technol. 53 (2019) 11932–11940, https://doi.org/10.1021/acs.est.9b04352.
[12] J. Yang, S. Jiang, W. Hu, H. Jiang, Highly efficient electrochemical dechlorination of florfenicol by an ultrathin molybdenum disulfide cathode, Chem. Eng. J. 427 (2022), 131600, https://doi.org/10.1016/j.cej.2021.131600.
[13] Y. Min, X. Zhou, J. Chen, W. Chen, F. Zhou, Z. Wang, J. Yang, C. Xiong, Y. Wang, F. Li, H. Yu, Y. Wu, Integrating single-cobalt-site and electric field of boron nitride in dechlorination electrocatalysts by bioinspired design, Nat. Commun. 12 (2021) 303, https://doi.org/10.1038/s41467-020-20619-w.
[14] Y. Luo, L. Xu, M. Rysz, Y. Wang, H. Zhang, P.J.J. Alvarez, Occurrence and transport of tetracycline, sulfonamide, quinolone, and macrolide antibiotics in the Haihe River Basin, China, Environ. Sci. Technol. 45 (2011) 1827–1833, https://doi.org/10.1021/es104009s.
[15] W. Xie, S. Yuan, X. Mao, W. Hu, P. Liao, M. Tong, A.N. Alshawabkeh, Electrocatalytic activity of Pd-loaded Ti/$TiO_2$ nanotubes cathode for TCE reduction in groundwater, Water Res. 47 (2013) 3573–3582, https://doi.org/10.1016/j.watres.2013.04.004.
[16] H. Yang, S. Zhang, W. Yang, X. Chen, Z. Zhuang, J. Xu, X. Wang, Molecular imprinted sol-gel nanotubes membrane for biochemical separations, J. Am. Chem. Soc. 126 (2004) 4054–4055, https://doi.org/10.1021/ja0389570.
[17] L. Ye, K. Mosbach, Molecular imprinting: synthetic materials as substitutes for biological antibodies and receptors, Chem. Mater. 20 (2008) 859–868, https://doi.org/10.1021/cm703190w.
[18] I. Bose, Y. Zhao, pH-controlled nanoparticle catalysts for highly selective tandem henry reaction from mixtures, ACS Catal. 10 (2020) 13973–13977, https://doi.org/10.1021/acscatal.0c03468.
[19] J. Cai, B. Niu, Q. Xie, N. Lu, S. Huang, G. Zhao, J. Zhao, Accurate removal of toxic organic pollutants from complex water matrices, Environ. Sci. Technol. 56 (2022) 2917–2935, https://doi.org/10.1021/acs.est.1c07824.
[20] X. Shen, L. Zhu, G. Liu, H. Yu, H. Tang, Enhanced photocatalytic degradation and selective removal of nitrophenols by using surface molecular imprinted titania, Environ. Sci. Technol. 42 (2008) 1687–1692, https://doi.org/10.1021/es071788p.
[21] S. Chai, Y. Wang, Y. Zhang, M. Liu, Y. Wang, G. Zhao, Selective electrocatalytic degradation of odorous mercaptans derived from S-Au bond recongnition on a dendritic gold/boron-doped diamond composite electrode, Environ. Sci. Technol. 51 (2017) 8067–8076, https://doi.org/10.1021/acs.est.7b00393.
[22] B. Niu, J. Cai, W. Song, G. Zhao, Novel electrochemical pretreatment for preferential removal of nonylphenol in industrial wastewater: biodegradability improvement and toxicity reduction, Environ. Sci. Technol. 54 (2020) 1258–1266, https://doi.org/10.1021/acs.est.9b03153.
[23] J. Chen, H. Tao, B. Liu, Unraveling the intrinsic structures that influence the transport of charges in $TiO_2$ electrodes, Adv. Energy Mater. 7 (2017), 1700886, https://doi.org/10.1002/aenm.201700886.
[24] Y. Ren, Z. Liu, F. Pourpoint, A.R. Armstrong, C.P. Grey, P.G. Bruce, Nanoparticulate $TiO_2$(B): An anode for lithium-ion batteries, Angew. Chem. Int. Ed. 51 (2012) 2164–2167, https://doi.org/10.1002/anie.201108300.
[25] X. Chen, S.S. Mao, Titanium dioxide nanomaterials: synthesis, properties, modifications, and applications, Chem. Rev. 107 (2007) 2891–2959, https://doi.org/10.1021/cr0500535.
[26] C. Liu, A. Zhang, D. Pei, H. Yu, Efficient electrochemical reduction of nitrobenzene by defect-engineered $TiO_{2-x}$ single crystal, Environ. Sci. Technol. 50 (2016) 5234–5242, https://doi.org/10.1021/acs.est.6b00730.
[27] C. Liu, Y. Min, A. Zhang, Y. Si, J. Chen, H. Yu, Electrochemical treatment of phenol-containing wastewater by facet-tailored $TiO_2$: efficiency, characteristics and mechanisms, Water Res. 165 (2019), 114980, https://doi.org/10.1016/j.watres.2019.114980.
[28] Y. Zhang, W. Dai, Y. Wen, G. Zhao, Efficient enantioselective degradation of the inactive (*S*)-herbicide dichlorprop on chiral molecular-imprinted $TiO_2$, Appl. Catal. B Environ. 212 (2017) 185–192, https://doi.org/10.1016/j.apcatb.2017.04.062.
[29] X. Han, Q. Kuang, M. Jin, Z. Xie, L. Zheng, Synthesis of titania nanosheets with a high percentage of exposed (001) facets and related photocatalytic properties, J. Am. Chem. Soc. 131 (2009) 3152–3153, https://doi.org/10.1021/ja8092373.
[30] Z. Zhang, Y. Li, M. Hu, A. Yu, Comparative transcriptome profiling reveals a mechanism of *Streptococcus agalactiae* resistance to florfenicol, Microb. Pathog. 142 (2020), 104098, https://doi.org/10.1016/j.micpath.2020.104098.
[31] Y.-P. Chen, S.-H. Lee, C.-H. Chou, H.-J. Tsai, Detection of florfenicol resistance genes in *Riemerella anatipestifer* isolated from ducks and geese, Vet. Microbiol. 154 (2012) 325–331, https://doi.org/10.1016/j.vetmic.2011.07.012.
[32] X. Chen, L. Liu, P.Y. Yu, S.S. Mao, Increasing solar absorption for photocatalysis with black hydrogenated titanium dioxide nanocrystals, Science 331 (2011) 746–750, https://doi.org/10.1126/science.1200448.
[33] G. Liu, H. Yang, H. Wang, L. Cheng, H. Lu, L. Wang, G. Liu, H. Cheng, Enhanced photoactivity of oxygen-deficient anatase $TiO_2$ sheets with dominant {001} facets, J. Phys. Chem. C 113 (2009) 21748–21788, https://doi.org/10.1021/jp907749r.

[34] Y. Wang, l Rao, P. Wang, Z. Shi, L. Zhang, Photocatalytic activity of N-$TiO_2$/O-doped N vacancy g-$C_3N_4$ and the intermediates toxicity evaluation under tetracycline hydrochloride and Cr(VI) coexistence environment, Appl. Catal. B Environ. 262 (2020), 118308, https://doi.org/10.1016/j.apcatb.2019.118308.
[35] L. Liu, Y. Jiang, H. Zhao, J. Chen, J. Cheng, K. Yang, Y. Li, Engineering coexposed {001} and {101} facets in oxygen-deficient TiO2 nanocrystals for enhanced $CO_2$ photoreduction under visible light, ACS Catal. 6 (2016) 1097–1108, https://doi.org/10.1021/acscatal.5b02098.
[36] W. Guo, Y. Qin, C. Liu, B. Guo, J. Zhou, Z. Xie, L. Wu, Unveiling the intermediates/pathways towards photocatalytic dechlorination of 3,3′,4,4′-trtrachlorobiphenyl over Pd /$TiO_2$(B) nanosheets, Appl. Catal. B Environ. 298 (2021), 120526, https://doi.org/10.1016/j.apcatb.2021.120526.
[37] W. Liao, J. Yang, H. Zhou, M. Murugananthan, Y. Zhang, Electrochemically self-doped $TiO_2$ nanotube arrays for efficient visible light photoelectrocatalytic degradation of contaminants, Electrochim. Acta 136 (2014) 310–317, https://doi.org/10.1016/j.electacta.2014.05.091.
[38] X. Chen, L. Liu, F. Huang, Black titanium dioxide ($TiO_2$) nanomaterials, Chem. Soc. Rev. 44 (2015) 1861–1885, https://doi.org/10.1039/C4CS00330F.
[39] E. Cossar, M.S.E. Houache, Z. Zhang, E.A. Baranova, Comparison of electrochemical active surface area methods for various nickel nanostructures, J. Electroanal. Chem. 870 (2020), 114246, https://doi.org/10.1016/j.jelechem.2020.114246.
[40] G. Jiang, M. Lan, Z. Zhang, X. Lv, Z. Lou, X. Xu, F. Dong, S. Zhang, Identification of active hydrogen species on palladium nanoparticles for an enhanced electrocatalytic hydrodechlorination of 2,4-dichlorophenol in water, Environ. Sci. Technol. 51 (2017) 7599–7605, https://doi.org/10.1021/acs.est.7b01128.
[41] Z. Lou, J. Xu, J. Zhou, K. Yang, Z. Cao, Y. Li, Y. Liu, L. Lou, X. Xu, Insight into atomic H* generation, $H_2$ evolution, and cathode potential of $MnO_2$ induced Pd/Ni foam cathode for electrocatalytic hydrodechlorination, Chem. Eng. J. 374 (2019) 211–220, https://doi.org/10.1016/j.cej.2019.05.171.
[42] R. Mao, N. Li, H. Lan, X. Zhao, H. Liu, J. Qu, M. Sun, Dechlorination of trichloroacetic acid using a noble metal-free graphene-Cu foam electrode via direct cathodic reduction and atomic H*, Environ. Sci. Technol. 50 (2016) 3829–3837, https://doi.org/10.1021/acs.est.5b05006.
[43] Q. Yao, X. Zhou, S. Xiao, J. Chen, I.A. Abdelhafeez, Z. Yu, H. Chu, Y. Zhang, Amorphous nickel phosphide as a noble metal-free cathode for electrochemical dechlorination, Water Res. 165 (2019), 114930, https://doi.org/10.1016/j.watres.2019.114930.
[44] G.V. Lowry, M. Reinhard, Pd-catalyzed TCE dechlorination in groundwater: solute effects, biological control, and oxidative catalyst regeneration, Environ. Sci. Technol. 34 (2000) 3217–3223, https://doi.org/10.1021/es991416j.
[45] B. Huang, J. Li, X. Cao, Y. Zhu, W. Chen, C. Lei, Electrochemical reduction of *p*-chloronitrobenzene(*p*-CNB) at silver cathode in dimethylformamide, Electrochim. Acta 296 (2019) 980–988, https://doi.org/10.1016/j.electacta.2018.11.125.
[46] Y. Xu, Z. Yao, Z. Mao, M. Shi, X. Zhang, F. Cheng, H. Yang, H. Tao, B. Liu, Single-Ni-atom catalyzes aqueous phase electrochemical reductive dechlorination reaction, Appl. Catal. B Environ. 277 (2020), 119057, https://doi.org/10.1016/j.apcatb.2020.119057.
[47] H. Yin, X. Cao, C. Lei, W. Chen, B. Huang, Insights into electroreductive dehalogenation mechanisms of chlorinated environmental pollutants, ChemElectroChem 7 (2020) 1825–1837, https://doi.org/10.1002/celc.202000067.
[48] H. Liu, Y. Ding, H. Tang, Y. Du, D. Zhang, Y. Tang, C. Liu, Electrocatalytic deep dehalogenation of florfenicol using Fe-doped CoP nanotubes array for blocking resistance gene expression and microbial inhibition during biochemical treatment, Water Res. 201 (2021), 117361, https://doi.org/10.1016/j.watres.2021.117361.
[49] X. Yang, X. Liu, S. Xie, J. Feng, J. Lv, The interaction between *Chlorococcum* sp. GD and indigenous bacteria in the process of municipal wastewater treatment, J. Clean. Prod. 362 (2022), 132472, https://doi.org/10.1016/j.jclepro.2022.132472.
[50] Y. Zhang, Z. Yang, Y. Xiang, R. Xu, Y. Zhang, Y. Lu, M. Jia, S. Sun, J. Cao, W. Xiong, Evolutions of antibiotic resistance genes (ARGs), class 1 integron-integrase (*intI*1) and potential hosts of ARGs during sludge anaerobic digestion with the iron nanoparticles addition, Sci. Total. Environ. 724 (2020), 138248, https://doi.org/10.1016/j.scitotenv.2020.138248.
[51] Y. Yang, X. Hu, X. Zhang, X. Chen, X. Wei, Z. Chen, H. Gu, S. Linghu, Y. Gao, Acclimatization of resorcinol results in microbial community dynamics and physicochemical characteristics of aerobic activated sludge, J. Clean. Prod. 364 (2022), 132467, https://doi.org/10.1016/j.jclepro.2022.132467.
[52] A. Táncsics, A.R. Szalay, M. Farkas, T. Benedek, S. Szoboszlay, I. Szabó, T. Lueders, Stable isotope probing of hypoxic toluene degradation at the Siklós aquifer reveals prominent role of *Rhodocyclaceae*, FEMS Microbiol. Ecol. 94 (2018), fiy088, https://doi.org/10.1093/femsec/fiy088.
[53] S. Jechalke, A.G. Franchini, F. Bastida, P. Bombach, M. Rosell, J. Seifet, M. V. Bergen, C. Vogt, H.H. Richnow, Analysis of structure, function, and activity of a benzene-degrading microbial community, FEMS Microbiol. Ecol. 85 (2013) 14–26, https://doi.org/10.1111/1574-6941.12090.
[54] N. Yan, M. An, J. Chu, L. Cao, G. Zhu, W. Wu, L. Wang, Y. Zhang, B.E. Rittmann, More rapid dechlorination of 2,4-dichlorophenol using acclimated bacteria, Bioresour. Technol. 326 (2021), 124738, https://doi.org/10.1016/j.biortech.2021.124738.